JOURNAL OF AIRCRAFT
Vol. 44, No. 1, January–February 2007

Gust Loads Alleviation Using Special Control Surfaces

B. Moulin* and M. Karpel†
Technion—Israel Institute of Technology, 32000 Haifa, Israel

DOI: 10.2514/1.19876

Control laws are designed for the alleviation of dynamic gust loads on a wind-tunnel model of a transport aircraft using wing-mounted control surfaces. Three different control surfaces are used: the symmetrically actuated main ailerons, special underwing forward-positioned control surfaces at about 0.8 of the wingspan, and special wing-tip forward-positioned control surfaces. The 5.3-m-span cable-mounted wind-tunnel model was constructed at the TsAGI laboratories and is being tested as there part of the 3AS 5th Framework European Commission research project. The length of a one-minus-cosine vertical gust velocity profile is tuned to yield maximal wing-root bending moment. All the control laws are based on simple low-pass filters for easy and robust application in the wind tunnel. Each is based on single input of a wing-tip accelerometer, which is shown to react sufficiently before the peak of the wing-root bending moment. All the three control means are shown to alleviate the extreme wing-root moments at intermediate design flight velocities by 9–16% and the wing-tip accelerations by 26–33%. The wing-tip control surface is found to be most effective, whereas the existing aileron least effective at these speeds. The existing ailerons become even less effective at higher speeds due to reduction in their aeroelastic effectiveness. They are also shown to be most problematic in creating aeroservoelastic instability when the gust-alleviation loop is closed. The effects of the designed control laws on the statistical response of the wing loads to continuous gusts are shown to be similar to their effects on discrete gusts.

Introduction

THE design of modern flight vehicles requires the evaluation of dynamic loads in response to discrete and random gust excitations [1]. Aviation regulations define design discrete gust profiles in a deterministic manner and continuous gust profiles in a stochastic manner. Control system can be used to reduce the dynamic response to gusts, and by that alleviate critical design loads and improve the ride comfort and equipment functionality

Common gust response procedures that do not conveniently include control system effects, such as that of MSC/NASTRAN [2], are based on second-order frequency-domain formulation. Modal frequency response functions are used in these procedures to calculate discrete transient gust response, via Fourier and inverse-Fourier transforms, and continuous gust response in rms terms via numerical integration of response power spectral density (PSD) functions. The main advantage of the frequency-domain approach is that it is based on oscillatory generalized aerodynamic force coefficient (AFC) matrices that can be generated by common, well-established, commercially available procedures such as the Doublet-Lattice method (DLM) [3] implemented in MSC/NASTRAN [2], and the constant pressure panel method (CPPM) [4] implemented in ZAERO [5]. A disadvantage of most existing frequency-domain procedures is that they are not conveniently adaptable to the consideration of aeroservoelastic (ASE) control system effects on the structural design gust loads, and to the inclusion of aeroelastic gust response considerations in the control-system design.

A common approach to ASE analysis is based on the conversion of the second-order aeroelastic equation of motion into first-order, state-space, constant-coefficient, time-domain equations of motion, which requires the approximation of the AFC matrices by rational functions in the Laplace domain. Rational approximation techniques such as the term-by-term Roger's approximation [6] and the more complicated but more efficient minimum-state method [7] are well established and commercially available. However, their application might involve some problems such as degraded accuracy, excessive number of augmenting states, or the need for careful parameterization, namely, loss of process robustness.

Two different formulation approaches to ASE gust response analyses were developed, evaluated, and compared in [8], and implemented in the GLOADS gust response module recently integrated in the ZAERO package [5]. The first is a first-order frequency-domain approach, which accommodates control systems in their most general state-space form, but with the AFC matrices still in their transcendental frequency-domain form. This option was intended for being used in industrial gust loads evaluation processes in which typically thousands of cases are evaluated in an automated manner, where robustness and compatibility with open-loop frequency-domain loads are of critical importance. The second approach is based on state-space time-domain formulation, which requires rational approximations of the generalized AFC matrices. This option was intended for cases where time-domain simulations, possibly with nonlinear effects, are required for the inclusion of the aeroelastic system in the control design process, and for application in design optimization processes, which are based on standard state-space formulation.

The discrete-gust formulation of [8] was adapted in [9] for efficient application in a realistic design environment, and applied to the calculation of dynamic loads in the design of the A400M military transport aircraft currently developed by EADS. The work presented in this paper was performed within the Active Aeroelastic Aircraft Structures (3AS) 5th Framework project of the European Commission for exploring the possibilities of using aeroelastic properties for obtaining better design of flight vehicles. The purpose of the work was the development of gust-loads alleviation control systems using specially designed wing control surfaces. The designed systems are to be applied to the 5.3-m-span cable-mounted EuRAM aeroelastic wind-tunnel model. The model was designed and built by the TsAGI aeronautical research laboratories in Russia, and is in the process of being tested in their wind tunnel as shown in Fig. 1.

Frequency-Domain Equations of Motion

The Laplace transform of the open-loop aeroelastic equation of motion in generalized coordinates, excited by control surface motion and atmospheric gusts, is

Received 4 September 2005; revision received 8 August 2006; accepted for publication 20 October 2006.

*Senior Researcher, Faculty of Aerospace Engineering. Member AIAA.
†Professor, Sanford Kaplan Chair in Aerospace Engineering, Faculty of Aerospace Engineering. Associate Fellow AIAA.

Fig. 1 EuRAM wind-tunnel model at TsAGI facilities.

$$([M_{hh}]s^2 + [B_{hh}]s + [K_{hh}] + q_\infty[Q_{hh}(s)])\{\xi(s)\} = -([M_{hc}]s^2 + q_\infty[Q_{hc}(s)])\{\delta_c(s)\} - \frac{q}{V}[Q_{hG}(s)]\{w_G(s)\} \quad (1)$$

where s is the Laplace variable, q_∞ is the dynamic pressure, V is the air velocity, the left-hand-side matrix coefficient matrices are the generalized mass, damping, stiffness, and AFC matrices associated with modal displacements $\{\xi(s)\}$, and the right-hand-side matrices are the generalized mass and aerodynamic forcing matrices due to control surface commanded deflections $\{\delta_c(s)\}$ and gust velocity vector $\{w_G(s)\}$. The AFC matrices $[Q_{hh}(s)]$, $[Q_{hc}(s)]$, and $[Q_{hG}(s)]$ can be calculated by unsteady aerodynamic codes at various tabulated reduced-frequency $k = \omega L/V$ values along the imaginary axis of the nondimensional Laplace variable $p \equiv sL/V = g + ik$, where L is a reference length and V is the true flight velocity.

To allow control systems of the most general forms, a first-order state-space formulation was suggested in [8] where the aerodynamic matrices keep their frequency-dependent form. The augmentation of the actuator states [5,7] yields the open-loop "plant" equations excited by the actuator inputs $\{\delta_c\}$. With state-space representation of the control system, the uncoupled plant and control equations can be expressed as

$$s\begin{Bmatrix} X_p \\ X_c \end{Bmatrix} = \begin{bmatrix} A_p(s) & 0 \\ 0 & A_c \end{bmatrix}\begin{Bmatrix} X_p \\ X_c \end{Bmatrix} + \begin{bmatrix} B_p & 0 \\ 0 & B_c \end{bmatrix}\begin{Bmatrix} u_p \\ u_c \end{Bmatrix} + \begin{bmatrix} B_{pw}(s) \\ 0 \end{bmatrix}\{w_G\}$$

$$\begin{Bmatrix} y_p \\ y_c \end{Bmatrix} = \begin{bmatrix} C_p(s) & 0 \\ 0 & C_c \end{bmatrix}\begin{Bmatrix} X_p \\ X_c \end{Bmatrix} + \begin{bmatrix} 0 & 0 \\ 0 & D_c \end{bmatrix}\begin{Bmatrix} u_p \\ u_c \end{Bmatrix} + \begin{bmatrix} C_{Gp}(s) \\ 0 \end{bmatrix}\{w_G\} \quad (2)$$

where the plant state vector is

$$\{X_p\}^T = \lfloor\, \xi^T \quad s\xi^T \quad \delta^T \quad s\delta^T \quad s^2\delta^T \,\rfloor$$

which includes the control actuator states and does not have aerodynamic lag states, and $\{X_c\}$ is the vector of states of the control system.

The ASE loop is closed by the application of the gain matrix:

$$\begin{Bmatrix} u_p \\ u_c \end{Bmatrix} = \begin{bmatrix} G_{pp} & G_{pc} \\ G_{cp} & G_{cc} \end{bmatrix}\begin{Bmatrix} y_p \\ y_c \end{Bmatrix} \quad (3)$$

The resulting closed-loop vehicle equation is

$$s\{X_v\} = [\bar{A}_v(s)]\{X_v\} + [\bar{B}_{vw}(s)]\{w_G\} \quad (4)$$

where

$$\{X_v\}^T = \lfloor\, X_p^T \quad X_c^T \,\rfloor$$

Modal response analysis to sinusoidal gust excitation can be performed by replacing s in Eq. (4) by $i\omega$, and interpolating for the generalized AFC matrices in $[A_p(i\omega)]$ of Eq. (2) from the tabulated $[Q_{hh}(ik)]$, $[Q_{hc}(ik)]$, and $[Q_{hG}(ik)]$ matrices of Eq. (1).

State-Space Time-Domain Equations of Motion

The time-domain ASE model for gust response analysis is based on the ASE model of [7], augmented by gust states, and excited by gust velocity inputs. The formulation is based on the gust modeling of [8]. The tabulated aeromatrices are first used for approximating the AFC matrix as a rational function of k in the entire frequency domain. An expansion to the entire Laplace domain is performed by replacing ik in the rational expression by the nondimensional Laplace variable p. The resulting Laplace domain approximation of

$$[Q_h] = \begin{bmatrix} Q_{hh} & Q_{hc} & Q_{hG} \end{bmatrix}$$

is

$$[\tilde{Q}_h(s)] = [A_0] + \frac{L}{V}[A_1]s + \frac{L^2}{V^2}[A_2]s^2 + [D]\left([I]s - \frac{V}{L}[R]\right)^{-1}[E]s \quad (5)$$

where the $[A_i]$ and $[E]$ matrices are column partitioned as

$$[A_i] = \begin{bmatrix} A_{hh_i} & A_{hc_i} & A_{hG_i} \end{bmatrix} \quad (i = 0, 1, 2),$$
$$[E] = \begin{bmatrix} E_h & E_c & E_G \end{bmatrix}$$

The resulting vehicle equation of motion, with the control system augmented, becomes

$$\{\dot{x}_v\} = [A_v]\{x_v\} + [B_v]\{u_v\} + [B_{vw}]\{\tilde{w}_G\}$$
$$\{y_v\} = [C_v]\{x_v\} + [D_v]\{u_v\} + [C_{Gv}]\{\tilde{w}_G\} \quad (6)$$

where

$$\{\tilde{w}_G\} = \begin{Bmatrix} w_G \\ \dot{w}_G \end{Bmatrix}$$

The equation of motion of the closed-loop aeroservoelastic system is, similarly to Eq. (4), of the form

$$\{\dot{x}_v\} = [\bar{A}_v]\{x_v\} + [\bar{B}_{vw}]\{\tilde{w}_G\} \quad (7a)$$

Output parameters that are not used by the control system but are of interest for dynamic response analysis can be defined as a separate vector $\{y_R\}$ and expressed in terms of the plant states and the gust inputs

$$\{y_R\} = [C_v]\{x_v\} + [C_{Gv}]\{\tilde{w}_G\} \quad (7b)$$

Discrete Gust Response

With the aerodynamic influence coefficient matrices defined in the frequency domain, a robust method for solving the aeroservoelastic response to discrete gusts is by using Fourier transforms [8], which avoids the need for rational aerodynamic approximations. The input gust excitation in Eq. (4) is replaced by its Fourier transform, frequency-domain modal response is calculated as described after Eq. (4), and response parameters of interest are then recovered from the modal response and transformed to the time domain by inverse Fourier transforms.

As discussed in the introduction section, some analysis, simulation, and design processes are based on the time-domain state-space Eqs. (7) that can be used for direct simulation of the time response to discrete gust excitation, performed by a straightforward numerical simulation. Once constructed, these equations are very efficient and can be used by standard simulation and control-design tool boxes such as Matlab. For clarity and simplicity, a single gust velocity profile is assumed in this section. The input vector $\{\tilde{w}_G(t)\}$ is based in this case on the user-defined gust velocity history $w_G(t)$ at the reference point x_0, and its derivative $\dot{w}_G(t)$. The modal response vectors $\{\xi(t)\}$ and $\{\dot{\xi}(t)\}$ are parts of the state vector obtained by the numerical integration. The modal acceleration response $\{\ddot{\xi}(t)\}$ is derived from the state vector by the second row block of Eq. (7).

The main disadvantage of the time-domain approach, relative to the Fourier-transform one, is that the state-space modeling process requires the unsteady aerodynamic force coefficient matrices to be approximated by rational functions of the Laplace variable; see Eq. (5). Any approximation might reduce the accuracy in subsequent analysis, relative to methods that do not require approximations. Nevertheless, the minimum-state approximation processes described in [7] and applied in [5] have been shown to be fairly robust and adequately accurate for typical aeroelastic stability and response applications when applied to the modal and control aeromatrices $[Q_{hh}(ik)]$ and $[Q_{hc}(ik)]$. However, rational approximations of the gust-related matrix $[Q_{hG}(ik)]$ might be problematic due to the high-frequency spiral nature of the gust terms when x_0 is located far ahead of some panels of the aeromodel. The solution for this problem is obtained in [8] by dividing the aerodynamic model into n_{zone} aerodynamic zones (i.e., sets of aerodynamic panels) each having its own reference point x_{0_i}. The replacement of a two-term gust input vector by a $2n_{\text{zone}}$-term vector does not yield significant difficulties in subsequent time simulations. However, it might create difficulties when used in continuous gust response, or in control design schemes. To return to a two-term-input situation, the time delays due to traveling from the first reference point to the others can be represented by approximate delay filters. Assuming two aerodynamic zones ($n_{\text{zone}} = 2$), the augmentation of an nth delay filter to the closed-loop Eq. (7) yields

$$\begin{Bmatrix} \dot{x}_v \\ \dot{x}_f \end{Bmatrix} = \begin{bmatrix} \bar{A}_v & \bar{B}_{vw_2} C_f \\ 0 & A_f \end{bmatrix} \begin{Bmatrix} x_v \\ x_f \end{Bmatrix} + \begin{bmatrix} \bar{B}_{vw_1} + \bar{B}_{vw_2} D_f \\ B_f \end{bmatrix} \{\tilde{w}_{G_1}\} \quad (8)$$

which has n states more than the original one. A delay approximation with $n = 3$ is typically accurate enough for gust response problems. With more than two aerodynamic zones, several delay filters can be connected to $\{\tilde{w}_{G_1}\}$ in parallel.

Design Loads

Net loads at extreme gust cases for structural design are often the primary purpose of the gust response analysis. Two methods are widely used for calculating dynamic loads [9], the mode-displacement (MD) method and the summation-of-forces (SOF) method, which is based on the classic mode-acceleration method. The MD method, which recovers the loads directly from the modal displacements, is more suitable for loads-alleviation control design. When used carefully in fairly well-distributed loads such as in gust excitation cases and with a sufficient number of modes taken into account, it can be used for calculating the actual loads as well [9]. The MD approach assumes that the modal superposition assumption used to construct the generalized aeroelastic equations of motion can also be used to recover the net-load distributions. The modal superposition assumption is

$$\{u_g(t)\} = [\phi_{gh}]\{\xi(t)\} \quad (9)$$

where $[\phi_{gh}]$ is the matrix of modal displacements. This assumption implies the vector net aerodynamic plus inertial loads expressed at the structural grid points is

$$\{F_{\text{MD}}(t)\} = [K_{gg}][\phi_{gh}]\{\xi(t)\} \quad (10)$$

where $[K_{gg}]$ is the discrete-coordinate stiffness matrix. The net loads can be integrated for obtaining section loads by the application of integration modes that can be calculated from the model geometry [5]. These modes, $[\phi_{gL}]$, are often referred to as "load modes." The resulting section loads, such as shear force , bending moment and torsion, are calculated by

$$\{L_{\text{MD}}(t)\} = [\phi_{gL}]^T[K_{gg}][\phi_{gh}]\{\xi(t)\} \quad (11)$$

where the product $[\phi_{gL}]^T[K_{gg}][\phi_{gh}]$ can be prepared when the model is constructed and used as the nonzero part of $[C_v]$ in Eq. (7b) for obtaining the section loads as the outputs of the ASE state-space equations, with $[C_{Gv}] = 0$.

Aeroelastic Models

The aircraft model with winglets and engines in upper position serves as the baseline configuration for this study. The gust-alleviation control of the baseline configuration is performed by using the existing main ailerons activated symmetrically. This configuration is referred to in this paper as the basic main aileron (BMA) configuration.

The structural beam-type MSC/NASTRAN model of the full wind-tunnel model was generated by TsAGI and updated to match the GVT results. The baseline half-model version that was used in this study is presented in Fig. 2. The associated ZAERO aerodynamic panel model is shown in Fig. 3. The aerodynamic model consists of eight aerodynamic panels representing the wing, aileron, horizontal and vertical tails, winglet, and engine pylons. The fuselage and the engines are presented by aerodynamic body macroelements.

The second control configuration is the baseline model with underwing control surfaces (UWC configuration). The control surfaces are connected to the wing through vertical pylons and forward horizontal stick holders. The wing-tip zones of the structural and aerodynamic models of the UWC configuration are shown in Figs. 4 and 5. The third control configuration is the baseline model with wing-tip control surfaces (WTC configuration). The control surfaces are connected to the wing-tip through horizontal forward

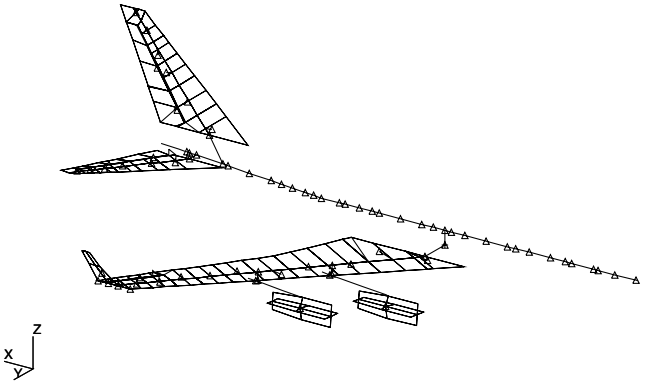

Fig. 2 Baseline structural model (BMA).

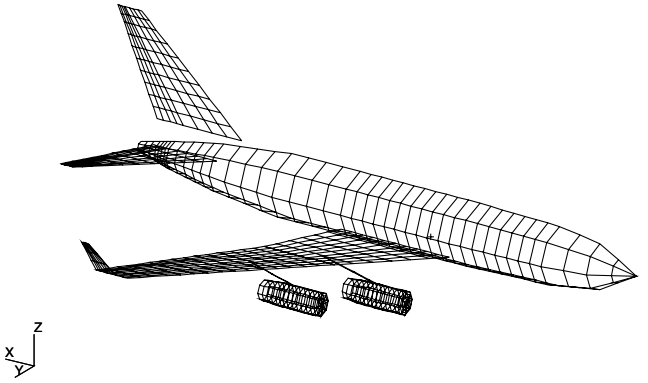

Fig. 3 Baseline aerodynamic model.

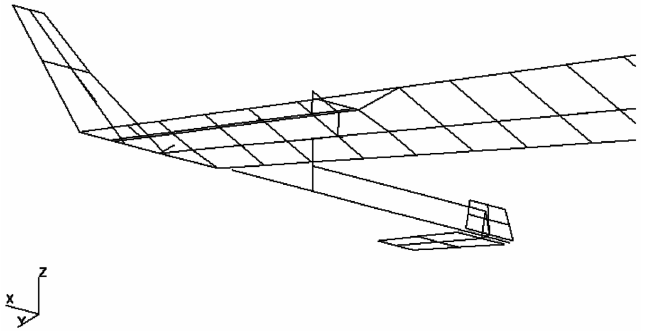

Fig. 4 Structural model of UWC.

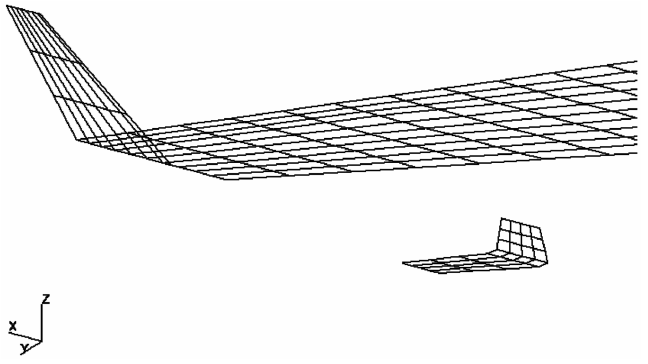

Fig. 5 Aerodynamic model of UWC.

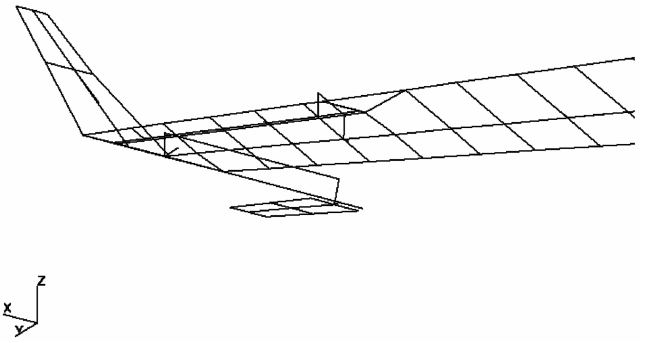

Fig. 6 Structural model of WTC.

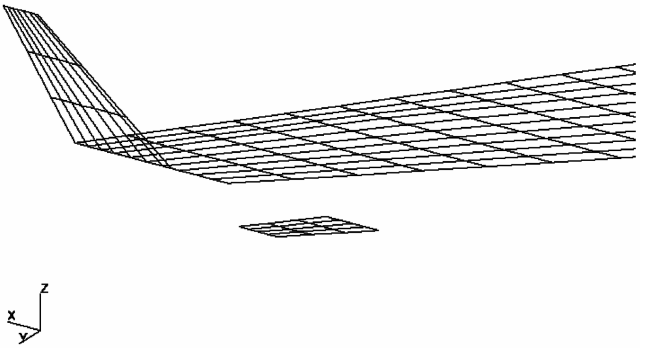

Fig. 7 Aerodynamic model of WTC.

stick holders. The wing-tip zones of the structural and aerodynamic models of the WTC configuration are shown in Figs. 6 and 7.

The gust vertical velocity is defined by the "1 − cos" profile

$$w_g(t) = \frac{\bar{w}_g}{2}\left(1 - \cos\frac{2\pi t}{L_g}\right) \tag{12}$$

where $\bar{w}_g$ is the maximal gust velocity, $\bar{w}_g = 1$ m/s in this study, and L_g is the gust length, in terms of the time for a point in the aircraft to travel across it. Open-loop gust response analysis was first performed for the BMA configuration for various gust length values at $V = 25$ m/s, sea level. This analysis was performed using the frequency-domain option of ZAERO with 35 structural modes taken into account in Eq. (2) with the control terms omitted. The resulting time histories of the wing-root bending moment are presented in Fig. 8. They demonstrate that the maximal bending moment is

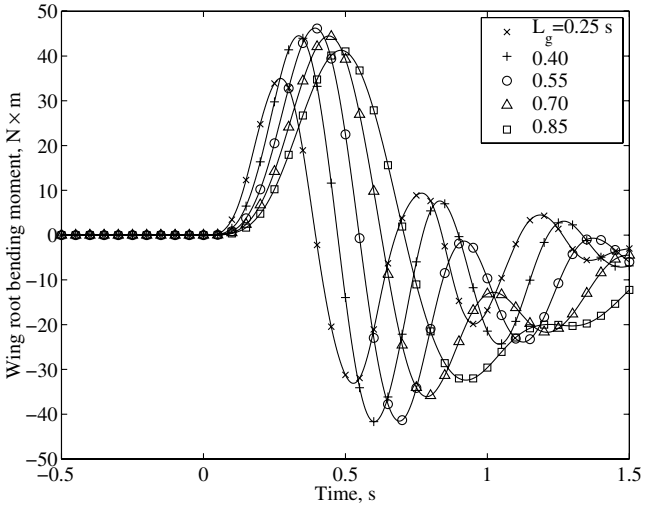

Fig. 8 Open-loop wing-root bending moment with various gust lengths.

obtained with $L_g = 0.55$ s, which coincides with the period of the first wing bending moment (1.8 Hz). Hence, subsequent analysis and control design are performed with $L_g = 0.55$ s.

The frequency-domain analysis was also used to check the accuracy of the state-space time-domain model that was constructed for the control design and the subsequent loads analyses. The state-space plant model was first obtained by augmentation of the open-loop aeroelastic model with the state-space model of the control-surface actuator.

The open-loop aeroelastic state-space model for the BMA configuration contains 70 structural states corresponding to the 35 structural modes and eight aerodynamic lag terms for the minimum-state aerodynamic approximation of Eq. (5), resulting in 78 states. The aerodynamic approximation of the gust column was sufficiently accurate with using one approximation zone, with the reference point located at the wing apex. The accuracy of the state-space model was checked by repeating the calculations of the wing loads of Fig. 8 with the time-domain Eq. (6) with the control terms omitted. The results by both methods were practically identical.

Each control surface configuration had one active hydraulic actuator in our study. All the actuators are stiff and powerful enough to be considered irreversible. They were modeled by a state-space realization of the third-order transfer function

$$T_{ac} = \frac{a_0}{s^3 + a_2 s^2 + a_1 s + a_0} \tag{13}$$

with $a_0 = 1.25 \times 10^7$, $a_1 = 1.5625 \times 10^5$, and $a_2 = 1144.0$, which is based on the second-order transfer function obtained from TsAGI and an additional low-pass filter with a pole at $s = -1000$ to yield the minimal order required for ASE modeling [7].

A wing-tip accelerometer was selected as a sensor for the control design of the BMA configuration. It is shown next that this acceleration signal is fast enough for significant alleviation of the loads peak. The accelerometers for the alternative UWC and WTC configurations were placed at the respective forward tips of the stick holders. The augmentation of the actuator model with the aeroelastic model resulted in an 81-state plant model with three inputs and five outputs. The inputs are the command to the actuator, the gust velocity $w_g(t)$, and $\dot{w}_g(t)$. The outputs are the accelerometer signal a_{wt}, the actuator output δ, the wing-root shear force F_z, bending moment M_x, and torsion moment M_y.

Design of Gust-Alleviation Control

The goal of the control design is to reduce the wing-root bending moment in response to discrete-gust excitation as much as possible without exceeding the maximal control-surface deflection (actuator output) of 8 deg, without degrading the wing-root torsion moment and shear force, and without causing instability within the tunnel velocity range of 0–40 m/s.

A simplistic design approach was taken to demonstrate the basic features of gust response alleviation using wing control surfaces, by analysis in this paper and later by wind-tunnel tests. Because the gust loads of interest are dominated by the response of the first wing bending mode (1.8 Hz in our case), the main two questions are whether the sensor can detect this response in time to activate the control surfaces before the loads reach their peaks, and whether the control surface can provide a significant relief. As will be demonstrated, the answers to both questions are positive. Based on these targets and features, the control design process was for defining the parameters of a low-pass filter for each configuration that rolls off well below the respective natural frequency of the control system.

The controller design was performed with respect to the defined discrete gust profile at $V = 25$ m/s, while checking the ASE stability (flutter) over the entire velocity range. The designed filters were then applied to closed-loop discrete and continuous gust response analyses at 25 and 35 m/s, for comparisons with the respective open-loop analyses.

The state-space aeroelastic plant model described earlier was exported by ZAERO for control design using Matlab for each control surface configuration separately. The control gains are expected to be significantly different mainly because of the different surface area: 0.045 m^2 of the aileron, 0.03 m^2 of the underwing surface, and 0.015 m^2 of the wing-tip surface. The Bode plot of the open-loop

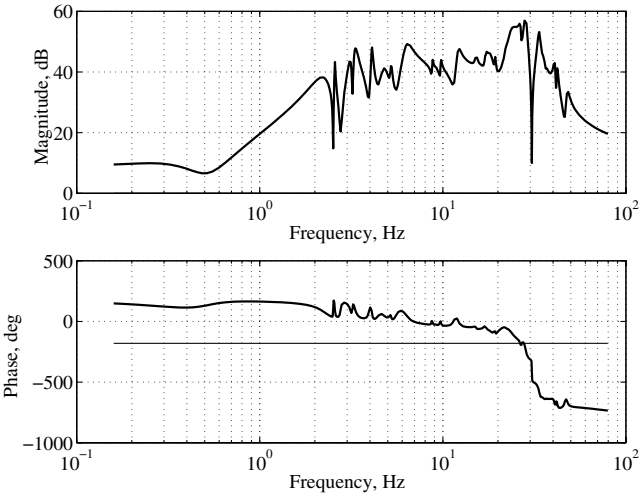

Fig. 9 Frequency response of wing-tip acceleration to aileron actuator command.

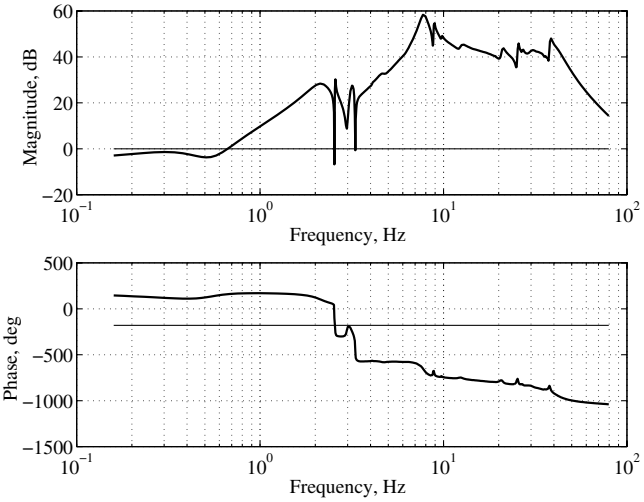

Fig. 10 Frequency response of UWC accelerometer to actuator command.

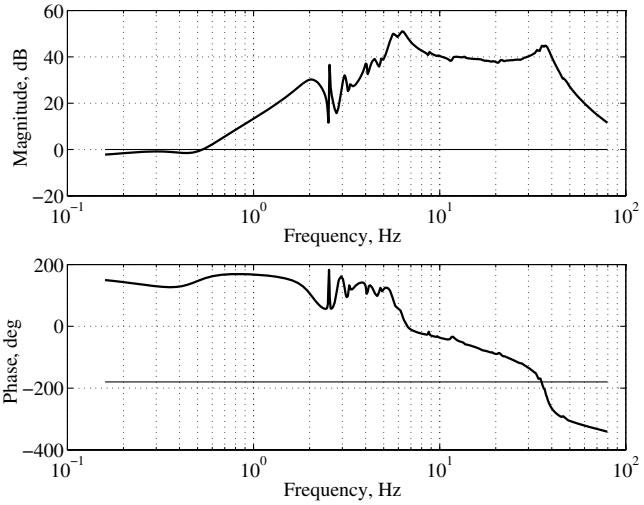

Fig. 11 Frequency response of WTC accelerometer to actuator command.

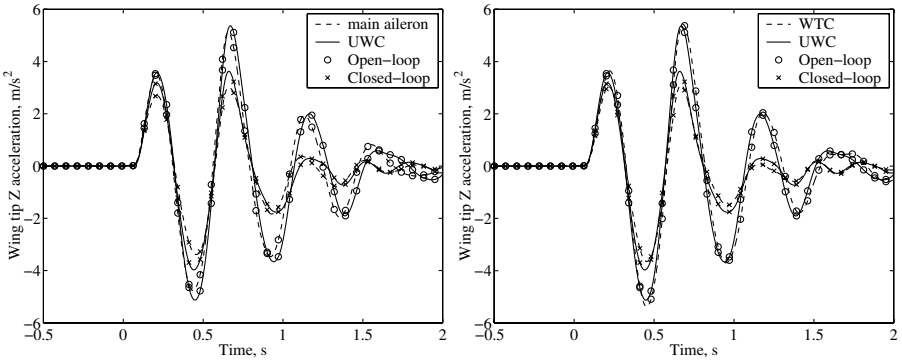

Fig. 12 Time histories of the acceleration signals of BMA, UWC, and TWC, $V = 25$ m/s.

response of the wing-tip accelerometer to sinusoidal actuator input is shown in Fig. 9. It shows that the accelerometer detects the important low-frequency motion but has excessive response at 24–28 Hz, which corresponds to structural modes with significant aileron rotation. Hence, a low-pass filter can be conveniently designed. It has the form of

$$T_c = k_c/(\tau_c s + 1) \tag{14}$$

Best alleviation which provides acceptable stability margins was obtained with $k_c = 0.09$ s^2/m and $\tau_c = 0.56$ s.

The control of the UWC configuration is based on symmetric application of the underwing control surfaces. An accelerometer was located at the nose of the underwing stick holder. The Bode plot of the open-loop response of the accelerometer at $V = 25$ m/s is shown in Fig. 10. It shows that the accelerometer detects the important low-frequency motion but has excessive response at 8.3–9 Hz, which corresponds to modes that involve significant bending of the stick holder. The peak at 39 Hz corresponds to the control surface rotation mode. Good control performance and marginal stability characteristics (shown later) could be obtained only with different control parameters of Eq. (14), $k_c = 0.17$ s^2/m, $\tau_c = 0.33$ s for $V = 25$ m/s, and $k_c = 0.17$ s^2/m, $\tau_c = 0.5$ s for $V = 35$ m/s.

The control of the WTC configuration is based on symmetric application of the wing-tip control surfaces. An accelerometer was located at the nose of the stick holder. The Bode plot of the open-loop response of the accelerometer at $V = 25$ m/s is shown in Fig. 11. It shows that the accelerometer detects the important low-frequency motion but has excessive response at 5.5–6.7 Hz, which corresponds to modes that involve significant bending of the stick holder. The peak 38 Hz corresponds to the control surface rotation mode. As in the BMA case, the same control parameters were used for both velocity points: $k_c = 0.17$ s^2/m, $\tau_c = 0.33$ s.

Comparison Between the Control Systems

The time histories of the open- and closed-loop acceleration signals for the BMA, UWC, and WTC configurations in response to the discrete gust excitation at $V = 25$ m/s are compared in Fig. 12. It can be observed that there are no significant differences between the three open-loop signals and between the three closed-loop ones, which means that the variation in accelerometer locations did not make much difference.

The time histories of the actuator outputs in the three closed-loop cases are compared in Fig. 13. It can be observed that there is a delay of about 0.15 s between the acceleration signals and the actuator response. If we add some delay in the aerodynamic response, we can deduce that the first peak of the control aerodynamic forces in each case is close in time to the first bending moment peak shown in Fig. 8 for the open-loop BMA case (with $L_g = 0.55$) and in Fig. 14. Also, the positive and negative peaks of the aileron rotations are close in time to the velocity peaks (the acceleration zero crossings), which provides significant damping. Consequently, the maximal acceleration responses, which occur in the second positive peak are reduced by about 38% when the loop is closed.

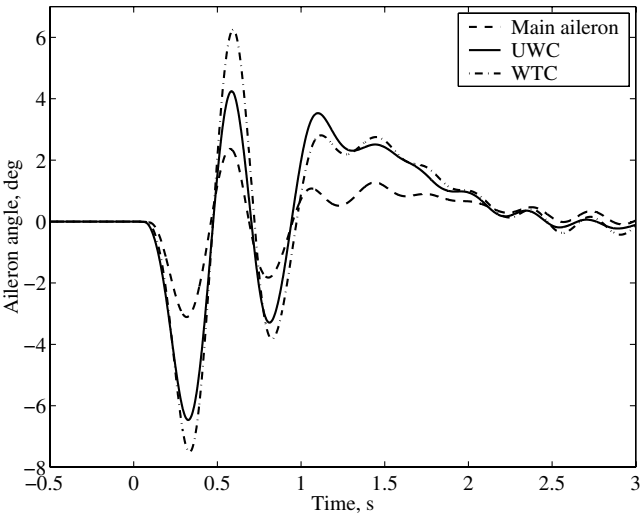

Fig. 13 Time histories of the closed-loop actuator output signals, $V = 25$ m/s.

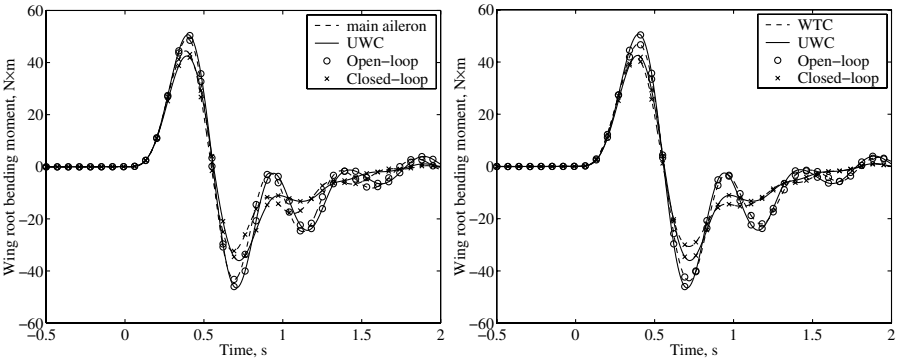

Fig. 14 Time histories of the wing-root bending for BMA, UWC, and TWC, $V = 25$ m/s.

Table 1 Maximal values of discrete gust response

Config.	Parameter	Parameter maximal value					
		$V = 25$ m/s			$V = 35$ m/s		
		Open	Closed	Diff. %	Open	Closed	Diff. %
BMA	M_x, N · m	49.06	44.46	−9.38	50.69	49.73	−1.89
	M_y, N · m	31.60	27.54	−12.8	32.59	30.08	−7.70
	F_z, N	33.11	33.14	0.09	38.11	40.32	5.80
	a_{wt}, m/s^2	5.126	3.386	−33.9	4.855	3.453	−28.9
	δ, deg	——	3.11	——	——	3.2	——
UWC	M_x, N · m	50.69	42.50	−16.2	52.72	42.33	−19.7
	M_y, N · m	31.92	27.95	−12.4	33.08	28.12	−15.0
	F_z, N	32.78	30.34	−7.44	37.67	35.63	−5.42
	a_{wt}, m/s^2	5.367	3.974	−26.0	5.210	3.315	−36.4
	δ, deg	——	6.46	——	——	4.67	——
WTC	M_x, N · m	46.92	41.66	−11.2	48.77	42.88	−12.1
	M_y, N · m	29.24	26.67	−8.79	30.45	27.99	−8.08
	F_z, N	31.51	31.66	0.48	37.00	37.86	2.32
	a_{wt}, m/s^2	5.422	3.648	−32.7	5.307	2.831	−46.7
	δ, deg	——	7.51	——	——	6.56	——

Table 2 Gain and phase margins at the actuator inputs

V, m/s	Config.	Gain margins, dB				Phase margins, deg			
		UGM	f_c, Hz	LGM	f_c, Hz	UPM	f_c, Hz	LPM	f_c, Hz
25	BMA	5.07	23.7	——	——	103	6.7	−113	2.6
	UWC	4.77	25.8	——	——	42	13.5	−104	2.6
	WTC	9.77	21.4	——	——	61	9.2	−84	2.6
35	BMA	7.19	18.0	——	——	79	7.9	−40	3.16
	UWC	4.27	2.5	——	——	42	13.1	−61	2.51
	WTC	5.36	19.3	——	——	37	13.1	−40	2.49

The time histories of the open- and closed-loop wing-root bending moments for the three configurations at $V = 25$ m/s are compared in Fig. 14. The presence alternative control surfaces affect the open-loop response in two ways: 1) loads are increased due to increased wing area, and 2) loads are reduced due to aeroelastic damping caused by the forward position of the added surfaces. These cause 1.5% increase in the maximal UWC bending moment and 4.2% reduction in the WTC case. The BMA, UWC, and WTC control laws reduce the maximal bending moment by 9.4, 13.3, and 15.1%, respectively, relative to the BMA open-loop case.

The maximal open- and closed-loop values of the wing-root bending moment, torsion and shear force, the acceleration signal, and

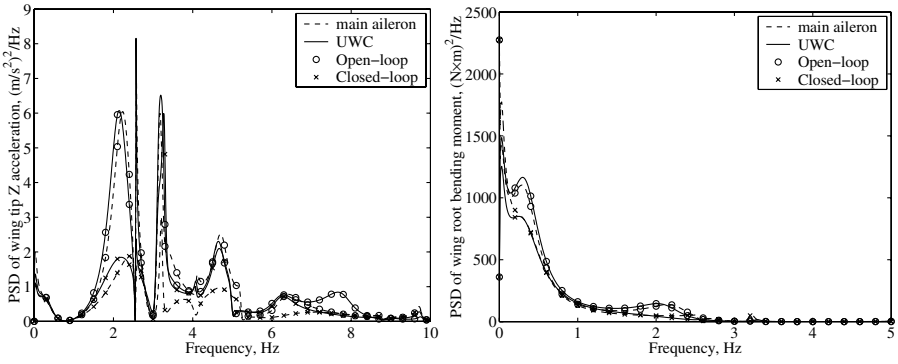

Fig. 15 PSD of the accelerations and bending moments of BMA and UWC, $V = 25$ m/s.

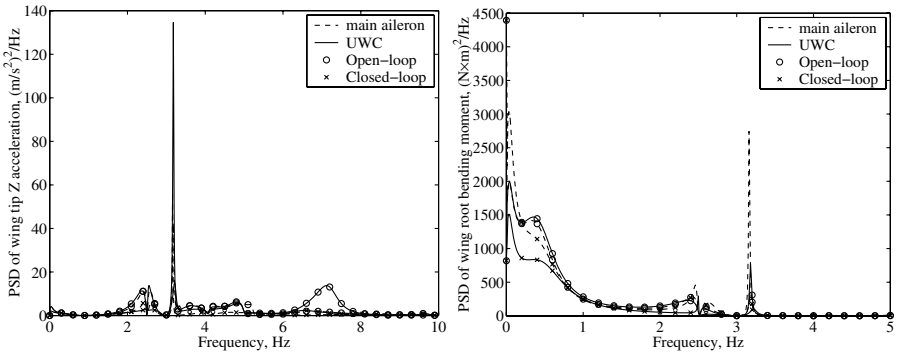

Fig. 16 PSD of the accelerations and bending moments of BMA and UWC, $V = 35$ m/s.

Table 3 RMS values of continuous gust response

Config.	Parameter	Parameter rms					
		$V = 25$ m/s			$V = 35$ m/s		
		Open	Closed	Diff. %	Open	Closed	Diff. %
BMA	M_x, N · m	29.01	27.08	−6.65	36.29	37.38	3.00
	M_y, N · m	18.92	17.25	−8.83	23.68	22.92	−3.21
	F_z, N	21.92	22.29	1.69	28.13	32.75	16.4
	a_{wt}, m/s^2	3.275	2.373	−27.5	5.072	3.650	−28.0
UWC	M_x, N · m	29.83	25.77	−13.6	52.72	29.82	−19.8
	M_y, N · m	18.93	17.14	−12.4	37.17	28.12	−13.6
	F_z, N	21.81	20.79	−4.68	28.99	28.31	−2.35
	a_{wt}, m/s^2	3.234	2.704	−16.4	5.979	4.108	−31.3
WTC	M_x, N · m	28.78	26.08	−9.38	35.76	31.93	−10.7
	M_y, N · m	18.14	16.85	−7.11	30.45	20.96	−6.60
	F_z, N	21.64	21.33	−1.43	28.90	30.26	4.71
	a_{wt}, m/s^2	3.035	2.354	−22.4	4.971	3.643	−26.7

the actuator output are given in Table 1 for the two design velocities. The percentage differences in this table are with respect to the open-loop values in the same line (unlike the aforementioned differences). The aileron (BMA) is not effective at the higher speed due to static aeroelastic effects, whereas the alternative forward control surfaces become more effective. In all cases, the actuator outputs are smaller than the limit (8 deg) because of stability constraints. Considering the ratio of the BMA, UWC, and WTC surface area, which is 3:2:1, it is clear that the alternative control surfaces are generally more efficient than the main ailerons, and the wing-tip surface is more effective than the underwing one. WTC also has less stability limitations in our study, as indicated by the control gain and phase margins summarized in Table 2.

The three control systems were also compared in continuous gust response performance. Analyses were performed using the frequency-domain option of ZAERO [5] at sea level for $V = 25$ m/s and $V = 35$ m/s with the rms value of the vertical gust velocity equal to 1 m/s and a gust scale of 100 m. PSD plots of the measured acceleration signal and the wing-root bending moment in the BMA and UWC cases are shown in Fig. 15 for $V = 25$ m/s and in Fig. 16 for $V = 35$ m/s. The sharp peak at 2.4 Hz, $V = 25$ m/s (Fig. 15) indicates a flutter mechanism that involved the wing bending and the inboard engine yaw modes, and becomes unstable at $V_F = 48$ m/s. This flutter mechanism is suppressed when the either the BMA or the UWC loops are closed. However, a new ASE flutter mechanism is created at 3.15 Hz that involves the outboard engine yaw and becomes unstable at $V_F = 40$ m/s. This mechanism, which becomes dominant at $V = 35$ m/s (Fig. 16), is the instability caused by the control gains limits discussed in the control design section. The large values at zero frequency in the bending moment plots stem from a singularity that does not affect the results.

Apart from the flutter mechanisms, it is clear from Figs. 15 and 16 that the gust-alleviation control reduces the gust response at most frequencies, especially around 2 Hz, for which it was designed. The loads around the short-period peak, at 0.3 Hz, are also suppressed, but it can be seen that the aileron becomes ineffective at $V = 35$ m/s, and even causes some bending moment increase at 2.3 Hz.

The rms values of the response parameters for the three control configurations (integrals of the PSD function) are summarized in Table 3. Here again, the presence of the underwing surface increases the bending moment response, whereas the wing-tip surface reduces it. It is also obvious that the aileron is ineffective at $V = 35$ m/s. The UWC performance appears to be slightly better than the WTC. However, if we consider the smaller area of the wing-tip surface, it is still somewhat favorable in the analyzed configuration.

Conclusions

Specially designed wing-mounted control surfaces have been shown to be capable of significantly reducing gust response loads acting on aircraft. A mathematical model of an aeroelastic wind-tunnel model was used for demonstrating the capabilities of symmetrically activated underwing and wing-tip, forward-mounted control surfaces in comparison with the regular ailerons. Frequency-domain formulation was used for open- and closed-loop loads analyses. State-space time-domain models were developed for the control design process. It was shown that wing-mounted accelerometers can be used effectively as single control inputs. A simple low-pass filter was used in each control case, provided physical insight, and allowed robust and easy applications in the planned wind-tunnel tests. The maximal wing-root bending moment was reduced by 9% with the ailerons, by 13% with the underwing surfaces, and by 16% with the wing-tip surfaces at intermediate velocities. The main ailerons became ineffective at high speeds, whereas the special surfaces became even more effective because of static aeroelastic effects. Flutter and control margin considerations provided critical constraints in the design process and limited the control gains. The controllers that were designed for a single discrete gust profile tuned to provide maximal bending moment demonstrated similar performances in response to statistical continuous gusts. The clear advantages of the special surfaces call for their evaluation in real aircraft designs. Considering the smaller size of the wing-tip surfaces, they were usually more effective then the underwing surfaces in the analyzed case. However, it is suggested to check the options in future designs.

Acknowledgments

The work presented in this paper was supported by the European Union through project G4RD-CT-2002-00679, Active Aeroelastic Aircraft Structures (3AS). The wind-tunnel model and the associated structural model were developed by Svetlana Kuzmina, Mikhail Zichenkov, Fanil Ishmuratov, and Vasily Chedrik of the Central Aerohydrodynamic Institute (TsAGI) in Russia. Adaptation of the structural model for aeroservoelastic analysis was performed by Vladimir Feldgun of the Technion—Israel Institute of Technology.

References

[1] Hoblit, F. M., *Gust Loads on Aircraft: Concepts and Applications*, AIAA Education Series, AIAA, Washington, DC, 1988.

[2] Rodden, W. P., and Johnson, E. H., *MSC/NASTRAN Aeroelastic Analysis User's Guide*, MacNeal–Schwendler, Los Angeles, 1994.

[3] Rodden, W. P., Taylor, P. F. and McIntosh, S. C., Jr., "Further Refinement of the Nonplanar Aspects of the Subsonic Doublet-Lattice Lifting Surface Method," *Journal of Aircraft*, Vol. 35, No. 5, 1998, pp. 720–727.

[4] Liu, D. D., Chen, P. C., Yao, Z. X. and Sarhaddi, D., "Recent Advances in Lifting Surface Methods," *The Aeronautical Journal*, Vol. 100, No. 998, Oct. 1996, pp. 327–339.

[5] ZAERO, Ver. 6.2 Theoretical Manual, ZONA 02-12.4, ZONA Technology, Inc., Scottsdale, AZ, Oct. 2002.

[6] Roger, K. L., "Airplane Math Modeling and Active Aeroelastic Control Design," AGARD CP-228, 1977, pp. 4.1–4.11.

[7] Karpel, M., "Time Domain Aeroservoelastic Modeling Using Weighted Unsteady Aerodynamic Forces," *Journal of Guidance, Control, and Dynamics*, Vol. 13, No. 1, 1990, pp. 30–37.

[8] Karpel, M., Moulin, B., and Chen, P. C., "Dynamic Response of Aeroservoelastic Systems to Gust Excitation," *Journal of Aircraft*, Vol. 42, No. 5, 2005, pp. 1264–1272.

[9] Karpel, M., Moulin, B., Anguita, L., Maderuelo, C., and Climent, H., "Aeroservoelastic Gust Response Analysis for the Design of Transport Aircrafts," AIAA Paper 2004-1592, April 2004.